High-Efficiency Nanoparticle Solution-Processed Cu(In,Ga)(S,Se)$_2$ Solar Cells

Alexander Eeles [ID], Panagiota Arnou, Jake W. Bowers [ID], John M. Walls, Stephen Whitelegg, Paul Kirkham, Cary Allen, Stuart Stubbs [ID], Zugang Liu, Ombretta Masala, Christopher Newman, and Nigel Pickett

Abstract—Thin film Cu(In,Ga)(S,Se)$_2$ -based (generally referred to as CIGS) solar cells represent a promising alternative to conventional crystalline silicon solar cells due to their high efficiencies, reduced cost, and better material utilization. In recent years, it has been demonstrated that it is possible to form thin films by annealing nanoparticulate material such that the nanoparticles coalesce to form large grained thin films. In this paper, we present a 13.8% efficient CIGS solar cell derived from printed nanoparticle inks. The approach was successfully extended to fabricate monolithic devices on larger substrates. These results demonstrate that low-cost, nonvacuum printing of CIGS nanoparticles has great potential to achieve high efficiencies and reduce the performance gap with the more traditional vacuum co-evaporation and sputtering techniques.

Index Terms—CIGS and CdTe thin film solar cells, nanoparticles, photovoltaic cells, thin film PV modules and manufacturing.

I. INTRODUCTION

THE photovoltaic market is currently dominated by silicon wafer-based solar cells [1]. In this type of solar cells, the active layer is made of single-crystal wafers produced by a process that involves fabricating and slicing high-purity, single-crystal silicon ingots. This process is expensive and although much of the manufacturing and module equipment has become standardized, the production of crystalline silicon solar cells remains cost-intensive and is characterized by relatively poor material utilization. The high cost of crystalline silicon wafers has prompted both industry and academia to investigate alternative

A. Eeles, P. Arnou, J. W. Bowers, and J. M. Walls are with the CREST, Wolfson School of Mechanical, Electrical and Manufacturing Engineering, Loughborough University, Loughborough LE11 3TU, U.K. (e-mail: a.eeles@lboro.ac.uk; P.Arnou@lboro.ac.uk; J.W.Bowers@lboro.ac.uk; J.M.Walls@lboro.ac.uk).

S. Whitelegg, P. Kirkham, C. Allen, S. Stubbs, O. Masala, C. Newman, and N. Pickett are with Nanoco Technologies Ltd., Manchester M13 9NT, U.K. (e-mail: SWhitelegg@nanocotechnologies.com; PKirkham@nanocotechnologies.com; carygallen@gmail.com; SStubbs@nanocotechnologies.com; OMasala@nanocotechnologies.com; CNewman@nanocotechnologies.com; NPickett@nanocotechnologies.com).

Z. Liu was with Nanoco Technologies Ltd., Manchester M13 9NT, U.K. He is now with the College of Optical and Electronic Technology, China Jiliang University, Hangzhou 310018, China (e-mail: ZLiu@nanocotechnologies.com).

Color versions of one or more of the figures in this paper are available online at http://ieeexplore.ieee.org.

materials for the development of high-efficiency thin film solar cells where material costs are significantly reduced compared to silicon. Semiconductor materials such as Cu(In,Ga)(S,Se)$_2$ (CIGS) are good candidates because they are strong light absorbers and have bandgaps that match well with the optimal spectral range for photovoltaic applications [2].

The champion power conversion efficiencies (PCEs) for CIGS solar cells have been achieved for devices where the absorber layer is deposited using vacuum-based processes such as co-evaporation and sputtering [3], [4]. While these techniques deliver high-quality films, they are difficult and expensive to scale to larger-area deposition and higher process throughput.

Solution-processed CIGS has attracted significant attention due to advantages in material utilization, yield, throughput, and cost reductions [5]. Printing technology has the potential to significantly reduce the cost of CIGS photovoltaic (PV) module manufacturing by replacing the standard, conventional vacuum-deposited technique. Printing processes, especially when implemented in a roll-to-roll processing framework, enable a much larger throughput. However, in order to be commercially competitive, it is essential for any alternative technology to achieve similar or superior efficiencies than those achieved by vacuum processing methods.

One approach to solution-processed CIGS is to chemically synthesize CIGS nanocrystals with controlled stoichiometry and crystal phase and disperse them in solvents, forming an ink or paste [6]. The nanoparticle ink can be deposited using low-cost printing techniques such as spin coating, slit coating, and blade coating to produce smooth, uniform absorber films. Another significant advantage of solution processing is that the ratio of the metals is fixed in the ink preparation and is independent of variation of the deposition thickness [2]. The ability to control the composition of the CIGS thin film is crucial because the optical and electrical properties of the CIGS absorber greatly depend on the composition.

In this paper, we report the fabrication of high-efficiency CIGS solar cells by using colloidal chalcopyrite CuIn$_x$Ga$_{1-x}$S$_2$ nanocrystals with a controlled In/Ga ratio to deposit uniform, crack-free micrometer-thick films. The nanocrystal films were annealed in a selenium atmosphere, which replaces sulfur with selenium and forms large, micron-sized, densely packed grains [7]. Solar cells fabricated using a standard soda-lime glass (SLG)/Mo/CIGS/CdS/intrinsic zinc oxide (i-ZnO)/indium tin oxide (ITO) structure achieved an in-house PCE of 13.8%. For a previous device with a nonoptimized grid area, a certified
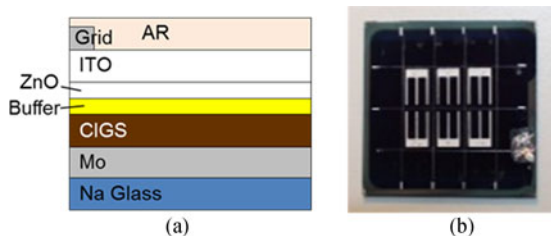
Fig. 1.   (a) Device schematic. (b) Image of completed device, 2.5 × 2.5 cm glass substrate with six device cells, each cell with total area approx. 0.27 cm^2 and active area approx. 0.2 cm^2.

PCE measurement of 12.69% was performed. This device had the highest active area PCE of 17.1% when the grid area was subtracted. It also had a low voltage deficit of 0.54 V. Larger devices were also fabricated and characterized showing the potential for the scalability of this approach. Finally, devices were also fabricated using a modified ink formulation, which reduced the required number of absorber coating steps from 6 to 3 without significantly affecting efficiencies.

II. EXPERIMENTAL DETAILS

The nanoparticle ink was synthesized using Nanoco's patented approach to grow nanoparticles [8]. The CuIn$_x$Ga$_{1-x}$S$_2$ nanoparticles were coated with octane thiol as an organic ligand, making them dispersible in common nonpolar organic solvents. In this case, nanoparticles were dissolved in toluene at a concentration of 200 mg/ml. The inks were prepared copper-rich [9], with Cu/(In + Ga) = 1.02 and with Ga/(Ga + In) = 0.33 determined using inductively coupled plasma (ICP) measurements. The S content within the nanoparticles is difficult to precisely quantify because of sulfur-containing ligands, but ICP measurements give S/Cu = 2.

A schematic for the device structure is shown in Fig. 1. Molybdenum was deposited on a soda lime glass by sputtering. The absorber layer was deposited in multiple layers by spin coating and annealing in a nitrogen atmosphere to remove the solvent and ligand. For the champion device, the absorber layer was deposited in six layers. A modified ink was also developed, which could be used to process devices with only three layers. No bandgap grading was intentionally built into the layers. The deposited absorber layers were etched with a solution of 10% KCN in deionized water. The devices were then selenized by placing them inside a graphite box with elemental selenium as a selenium source and annealing in a carbolite split tube furnace. The selenization was performed under a constant flow of N_2 at just above atmospheric pressure. A 50 nm CdS buffer layer was deposited using chemical bath deposition following the method from [10]. A total of 50 nm of i-ZnO and 350 nm of ITO were deposited by magnetron sputtering. Metal grids and a MgF$_2$ antireflection layer were deposited by thermal evaporation, followed by a further conditioning step. The substrate was mechanically scribed into individual cells. Certified *IV* measurements were performed at the CREST photovoltaic measurement and calibration laboratory, which is now an ISO 17025:2005 accredited laboratory (lab number 9171). All other *IV* measurements were performed using a Newport 9100 solar simulator, operating at
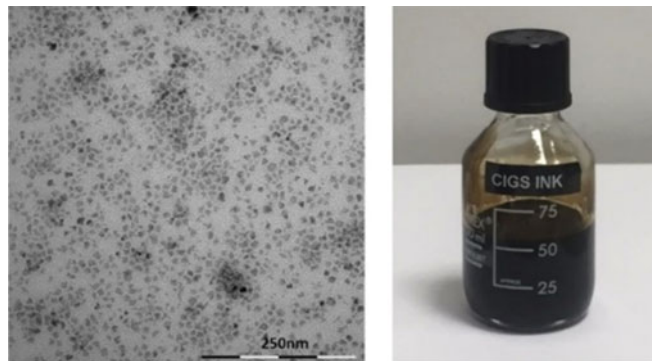

Fig. 2.   TEM image of the CIGS nanoparticles (left) and a photograph of the nanoparticle ink (right).

AM1.5G (1 kW/m^2), as calibrated using a 91150 V Reference Cell from Newport. The connection to the devices was made using 3 M clips and the *IV* measurement made using a Keithley 2400. No active cooling was applied to the device during measurement. Area measurement was made using an optical microscope. External quantum efficiency (EQE) measurements were made using a Bentham PVE300 dual source spectral response measurement system. Cross sections were imaged using a Carl Zeiss 1530 VP field emission gun scanning electron microscope (SEM). Electroluminescence (EL) measurements were made using a Si CCD camera. A constant bias voltage of 4 V was used for the excitation with an exposure time of 120 s. Multispectral laser beam induced current (LBIC) images were made using an in-house developed measurement system with 11 different wavelength lasers focused onto a single point [11].

III. RESULTS

A. Nanoparticle Ink

CIGS nanoparticles were synthesized using a solution approach that produces relatively small (<50 nm) nanoparticles. Different sized nanoparticles can be synthesized using this method. Fig. 2 shows a transmission electron microscopy (TEM) image of CIGS nanoparticles with an average diameter of 15 nm and the visual appearance of the resulting ink. The method produces pure chalcopyrite CIGS nanoparticles free of secondary phases such as binary Cu$_{2-x}$Se phases. The presence of such impurities at the CIGS surfaces of the deposited film negatively affects PCEs of photovoltaic cells. Given the slightly copper-rich nanoparticle precursor, the final film would normally be expected to contain Cu$_{2-x}$Se phases. A reduction in the Cu content of the film may be occurring during the KCN etch, but there are insufficient data to confirm this.

The nanoparticles are capped with an organic ligand that has high volatility, so it can be removed easily during the sintering process, reducing the risk of incorporating carbon impurities in the sintered films.

Due to the presence of the organic ligand on the surface of the nanoparticles, versatile inks can be created by dispersing the nanoparticles in a range of solvents. The ink can be deposited on the substrate by various deposition techniques including spin-coating, blade coating, and spraying. The devices described
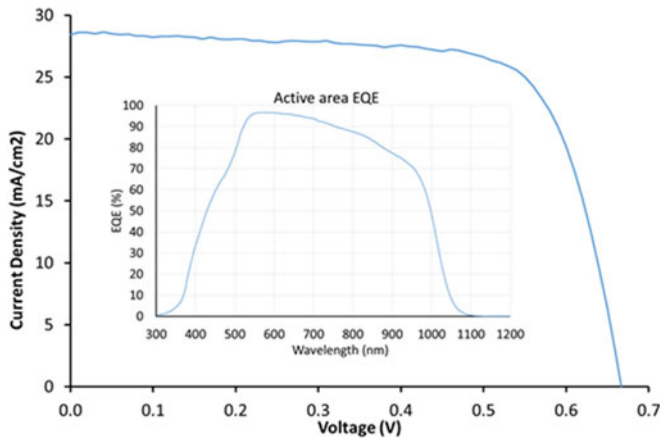
Fig. 3.   *J–V* measurement for the 13.8% PCE device.

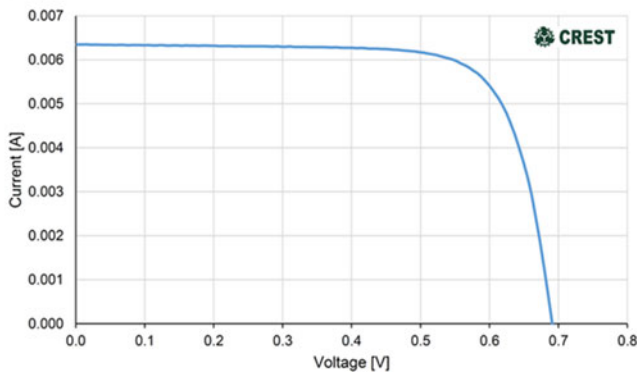| Performance corrected to given test conditions			
Parameter	Value	U (k=2) Unit	U (k=2)
Short Circuit Current (I_{SC})	6.35 ±0.13	[mA]	2.04 %
Open Circuit Voltage (V_{OC})	690.78 ±2.42	[mV]	0.35 %
Fill Factor (FF)	75.76 ±0.38	[%]	0.50 %
Maximum Power Output (P_{MP})	3.32 ±0.07	[mW]	2.15 %
Cell Efficiency (Eff)	12.69 ±0.31	[%]	2.48 %

Fig. 4.   *J–V* measurement for the best performing device. Certified by CREST Photovoltaic Measurement and Calibration Laboratory.

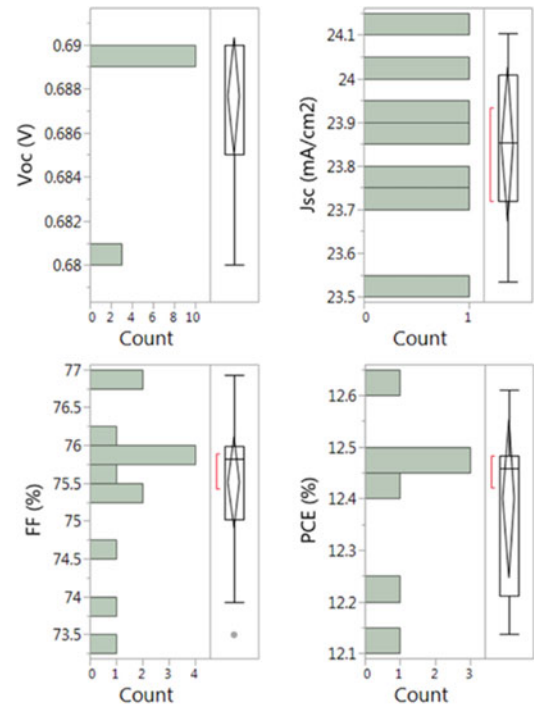Fig. 5.   Distribution of device characteristics from in-house measurements.
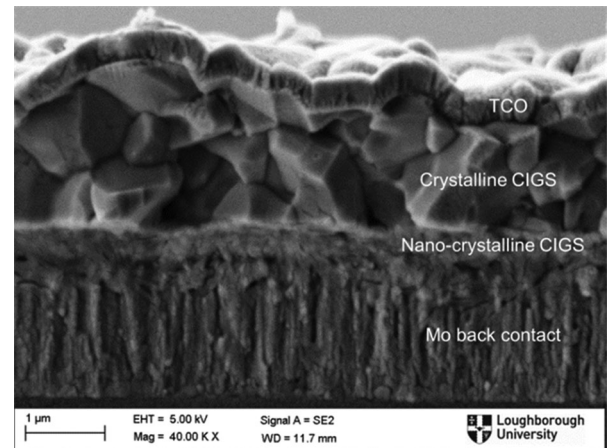
Fig. 6.   Cross-sectional SEM images taken from a 16 cm^2 minimodule.

in this paper were fabricated by spin coating the ink on conventional low-cost SLG substrates.

B. Champion Devices

The highest total area PCE achieved was 13.8% on a 0.45 cm^2 device. This device had V_{oc}, J_{sc}, and FF of 0.67 V, 28.4 mA/ cm^2, and 72.4%, respectively. The *IV* and EQE curves for this device can be seen in Fig. 3. The bandgap was measured as 1.22 eV using the maximum of the derivative of the EQE. The curve shows a high spectral response up to the band gap and the short-circuit current density indicates good charge generation and collection in the absorber.

A certified measurement (see Fig. 4) has been made for a smaller device, which was made before grid optimization. This device achieved a 12.69% total area PCE, which corresponds to 17.17%-active area PCE when the shadowed area of the grid is taken into account (total area 26.15 mm^2, active area 19.33 mm^2). Almost identical results were obtained using the

in-house measurement system (within error) indicating a minimum measurement system bias.

The large difference between active area and total area is due to nonoptimized grid designs; however, the quality of the device can also be seen from the voltage deficit ($E_g - V_{oc}$) of only 0.54 V, which is comparable to vacuum-based techniques without Ga gradients, indicating the formation of high-quality crystals with good electronic properties.

The distribution of the efficiencies from a run of 12 of these nominally 0.27 cm^2 devices is shown in Fig. 5.

Devices display a double-layered absorber structure, with a highly recrystallized top layer and a nanocrystalline bottom layer (see Fig. 6).

This structure is similar to many other reported solution-processed devices [7], [12], [13]. However, the recrystallized region dominates with a much smaller nanocrystalline region.
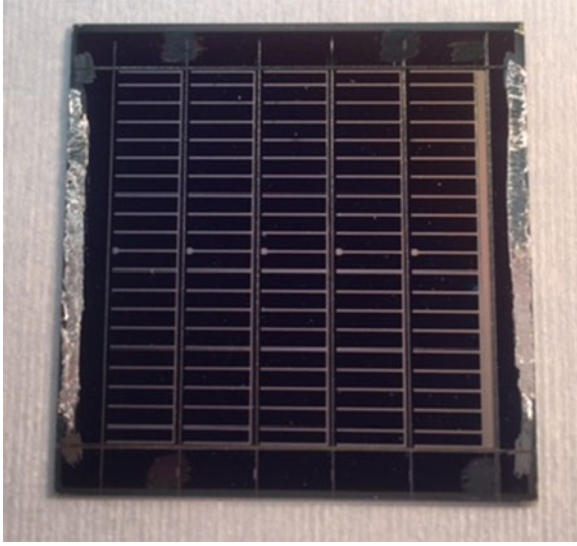
Fig. 7. Digital photograph of five cell monolithic integrated minimodule on a $5 \times 5\,\text{cm}^2$ glass substrate with an aperture area of $16\,\text{cm}^2$, fabricated with the nanoparticle ink.

Secondary ion mass spectrometry data from samples representative of the champion device show no indication of either Ga or S gradients in the device. In addition, the minimum bandgap estimate agrees with that estimated from the average Ga content, whereas it should be lower if Ga grading were present.

C. Reduction of the Number of Absorber Deposition Steps

One of the challenges in achieving high efficiency is forming dense, crack-free absorber films. In general, multiple coatings are necessary to avoid the formation of cracks. A reduction in the number of coatings is advantageous for larger area devices because it can speed-up the fabrication process and maximize material utilization. We found that the composition of the ink is crucial to achieving a crack-free film with the least possible number of coatings. With the ink made purely of quaternary CIGS nanoparticles, six coatings were necessary to obtain crack-free films with $>1.5\,\mu\text{m}$ thickness. When the CIGS nanoparticles were combined with other chalcogenide nanoparticles, uniform, crack-free micrometer-thick films could be obtained in a single coating step. With spin coating these films were nonuniform due to the low spin speed required; therefore, devices were fabricated with three coating steps. Small area ($0.27\,\text{cm}^2$) devices were fabricated with the blended ink with three coating steps showing similar efficiencies to the devices fabricated with the pure CIGS nanoparticles in a multicoating process.

D. Minimodule Fabrication

As an intermediate step toward full-scale commercial modules, five cell minimodules of aperture area $16\,\text{cm}^2$ (area including scribe lines and grid) on $5\,\text{cm} \times 5\,\text{cm}$ SLG substrates were developed, as shown in Fig. 7.

The interconnects between the cells were made using conventional scribing techniques with p1, p2, and p3 scribe lines. The p1 scribe lines for the devices were laser cut before deposition of
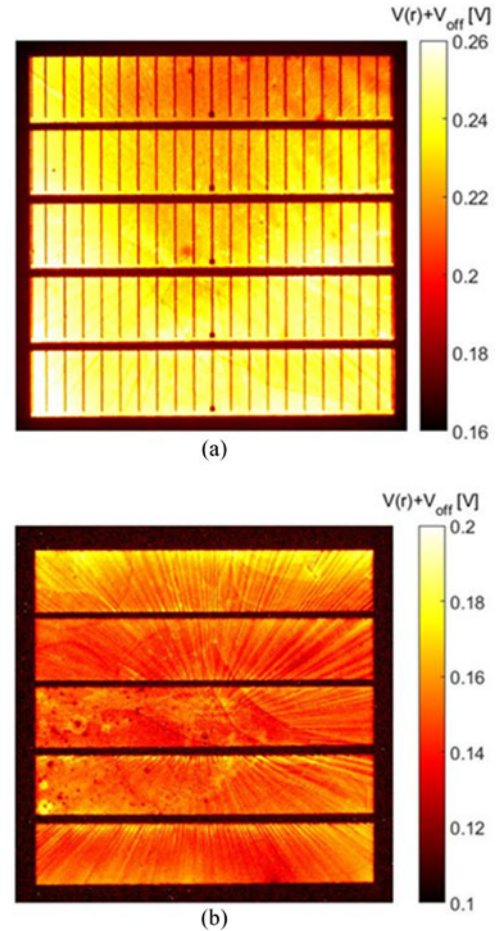

Fig. 8. Electroluminescence images of 5 cell minimodules. (a) A gridded device, which gave the highest efficiency of 9.6%. (b) Ungridded device.

the absorber layer. The p2 and p3 scribe lines were cut mechanically by hand. The hand scribing of the lines was performed to demonstrate the scalability of this technique. However, this method forms much more widely spaced scribe lines than could be achieved in production. Monolithic devices were prepared both with and without grids.

It was found that the contact resistance between the Ag grid and the back contact was significantly lower than that for the transparent conductive oxide (TCO)–back contact connection. Therefore, in the devices with grids, the p3 scribe was performed after TCO deposition. The gridded devices have a much lower series resistance than the nongridded devices and the corresponding increase in the FF more than compensated for the reduction in J_{sc} due to shadowing from the grid. The highest performing device had an aperture area efficiency $= 9.6\%$, $V_{\text{oc}} = 3.09\,\text{V}$, $J_{\text{sc}} = 4.26\,\text{mA/cm}^2$, and FF $= 72.9\%$.

Fig. 8 shows electroluminescence images of the two device formats. The camera signal for the images has been converted to a relative voltage scale using the following [14]:

$$V(r) + V_{\text{off}} = \frac{kT}{q}\ln\left(S_{\text{cam}}\right). \qquad (1)$$
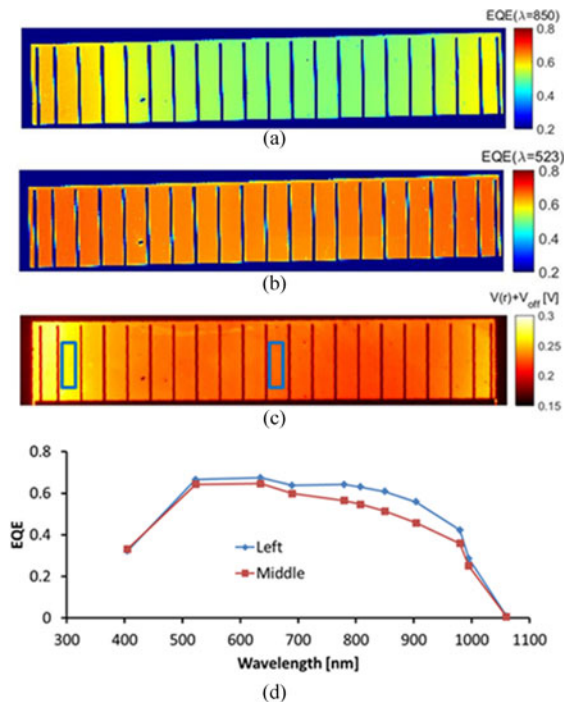
Fig. 9. (a) LBIC image from 850 nm laser. (b) LBIC image from 523 nm laser. (c) EL image. (d) EQE extracted from the multispectra LBIC data in two different areas of the cell, as indicated by the blue boxes in the EL image.

The image intensity on this scale is approximately equal to the junction voltage at that point plus a constant offset voltage.

One striking feature of the electroluminescence images is the "comet tracks," which are an artifact of the spin coating of the absorber layer and are not visible by eye. The comet tracks are much more pronounced in the minimodules than the $0.27\,\mathrm{cm}^2$ cells since they are generated strongly by the p1 scribe lines. It is expected that this problem should be resolved by using more appropriate coating techniques such as blade coating or spraying.

Another form of nonuniformity can be observed on some devices. For the gridded device in Fig. 8, this can be seen as a U-shaped area in the top half of the device with relatively weaker emission.

Fig. 9 shows multispectral LBIC measurement along with EL measurements from one cell of a minimodule.

It shows that the dimmer areas in the EL image have reduced long wavelength EQE, indicating that a reduced fraction of the absorber layer has fully recrystallized. The absorber recrystallization is linked to the selenization parameters and we believed that this nonuniformity is caused by the gas flow in the selenization tube, which was optimized for the 2.5×2.5 cm substrates. It should be possible to significantly improve the selenization uniformity by optimizing the process parameters.

Minimodules were produced using both the 6-step and 2-step ink deposition methods. Despite the observed nonuniformities, the aperture area PCE achieved with the minimodules was ∼10%. The PCE can be significantly improved by reducing the excessively large area of the scribe lines, which was due to the manual scribing and improving the uniformity of the final device.

IV. CONCLUSION

We present a process for the fabrication of highly efficient CIGS solar cells using nonvacuum techniques based on the conversion of CIGS nanoparticles into the absorber film. The utility of this technology is demonstrated by the fabrication of laboratory scale solar cells with a 13.8% PCE, using a standard CIGS device structure. With an active area PCE > 17% demonstrated, larger total area PCE values are possible with further optimization. The industrial applicability of this approach was demonstrated by producing minimodules with ∼10% aperture area efficiency, with scope for easy further improvements. This approach is promising for a high-throughput and high-yield process for low-cost thin films solar cell fabrication.

REFERENCES

[1] C. Battaglia, A. Cuevas, and S. De Wolf, "High-efficiency crystalline silicon solar cells: Status and perspectives," *Energy Environ. Sci.*, vol. 9, no. 5, pp. 1552–1576, 2016.
[2] M. Kemell, M. Ritala, and M. Leskelä, "Thin film deposition methods for CuInSe2 solar cells," *Crit. Rev. Solid State Mater. Sci.*, vol. 30, no. 1, pp. 1–31, 2005.
[3] P. Jackson *et al.*, "Properties of Cu(In,Ga)Se2 solar cells with new record efficiencies up to 21.7%," *Phys. Status Solidi, Rapid Res. Lett.*, vol. 9, no. 1, pp. 28–31, 2015.
[4] P. Jackson *et al.*, "Effects of heavy alkali elements in Cu(In,Ga)Se2 solar cells with efficiencies up to 22.6%," *Phys. Status Solidi, Rapid Res. Lett.*, vol. 10, no. 8, pp. 583–586, Aug. 2016.
[5] H. Azimi, Y. Hou, and C. J. Brabec, "Towards low-cost, environmentally friendly printed chalcopyrite and kesterite solar cells," *Energy Environ. Sci.*, vol. 7, no. 6, pp. 1829–1849, 2014.
[6] H. W. Hill and M. C. Beard, "Solar cells from colloidal nanocrystals: Fundamentals, materials, devices, and economics," *Curr. Opinion Colloid Interface Sci.*, vol. 14, no. 4. pp. 245–259, 2009.
[7] Q. Guo, G. M. Ford, H. W. Hillhouse, and R. Agrawal, "Sulfide nanocrystal inks for dense $Cu(In_{1-x}Ga_x)(S_{1-y}Se_y)_2$ absorber films and their photovoltaic performance," *Nano Lett.*, vol. 9, no. 8, pp. 3060–3065, Aug. 2009.
[8] J. Harris, C. Newman, O. Masala, L. Wylde, and N. Pickett, "Copper-indium-gallium-chalcogenide nanoparticle precursors for thin-film solar cells," U.S. Patent 9 466 743, Sep. 12, 2014.
[9] C. Newman, O. Masala, P. Kirkham, C. Allen, and S. Whitelegg, "Preparation of copper-rich copper indium (Gallium) diselenide/disulphide nanoparticles," U.S. Patent 20 150 136 213, May 21, 2015.
[10] M. A. Contreras *et al.*, "Optimization of CBD CdS process in high-efficiency Cu (In, Ga) Se 2-based solar cells," *J. Nanosci. Technol.*, vol. 404, pp. 204–211, 2002.
[11] R. Gottschalg *et al.*, "Spatially and spectrally resolved electroluminescence measurement system for photovoltaic characterisation," *IET Renew. Power Gener.*, vol. 9, no. 5, pp. 446–452, Jul. 2015.
[12] P. Arnou *et al.*, "Solution processing of CuIn(S,Se)2 and Cu(In,Ga)(S,Se)2 thin film solar cells using metal chalcogenide precursors," *Thin Solid Films*, vol. 663, pp. 76–80, 2016.
[13] A. R. Uhl *et al.*, "Liquid selenium enhanced grain growth of nanoparticle precursor layers for CuInSe2 solar cell absorbers," *Prog. Photovolt. Res. Appl.*, vol. 23, no. 9, pp. 1110–1119,x Sep. 2015.
[14] A. Helbig, T. Kirchartz, R. Schaeffler, J. H. Werner, and U. Rau, "Quantitative electroluminescence analysis of resistive losses in Cu(In, Ga)Se2 thin-film modules," *Sol. Energy Mater. Sol. Cells*, vol. 94, no. 6, pp. 979–984, 2010.

Authors' photographs and biographies not available at the time of publication.